Metals

Competition between intragranular and intergranular deformation mechanisms in ODS ferritic steels during hot deformation at high strain rate

D. L. Sornin[1,*], A. Karch[1], and R. E. Logé[2]

[1] DEN, Service de Recherches Métallurgiques Appliquées, CEA, Université Paris-Saclay, 91191 Gif-sur-Yvette, France
[2] LMTM, EPFL, Material Institute, PX Group Chair, Rue de la Maladiére 71b-CP526, 2002 Neuchâtel, Switzerland

ABSTRACT

Oxide Dispersed Strengthened (ODS) ferritic stainless steels present well-known fine grains microstructures where dislocation movement is hindered by a dense precipitation of nano-oxides particles. Previous research, on the thermomechanical behavior at high temperature and strain rates, was focused on torsion tests (Karch in J Nucl Mater 459:53–61, 2014). Considering texture evolution and grain shape as indicators of the intragranular dislocation glide activity, it was shown that, for high temperature and strain rate, intragranular deformation was in competition with intergranular accommodation. The latter phenomenon was related to early damaging at grain boundaries. The occurrence of a transition phenomenon from an intragranular to an intergranular deformation mechanism, with increasing temperature, was recently confirmed by neutron diffraction spectroscopy (Stoica in Nature Commun 5:5178, 2014). In the present paper, hot extrusion (HE) tests are performed, avoiding damage due to the high stress triaxiality, and allowing further investigation of intragranular and intergranular plasticity at large strains. Three ferritic steels exhibiting various precipitation size and density were hot extruded. Microstructure evolution at different stages of deformation is investigated using the Electron Back-Scattered Diffraction (EBSD) technique. After extrusion at 1373 K (1100 °C), the microstructure of ODS steels consists of a mixture of small round shape grains and larger elongated grains containing low-angle grain boundaries. Texture measurements show the appearance of the α-fiber (<110>//extrusion direction) and an increase in its intensity during the extrusion process in the larger grains. The fragmentation of the large elongated grains by Continuous Dynamic Recrystallization (CDRX) partially occurs in ODS materials depending on precipitation reinforcement. For smaller grains, plastic deformation has no effect on crystallographic orientation and grain shape, indicating a grain boundary accommodation phenomenon as the major deformation mechanism. Precipitation density not only impacts the intragranular dislocation glide activity, but also reduces CDRX kinetics in coarse grains.

Address correspondence to E-mail: denis.sornin@cea.fr

Introduction

The coming Gen IV nuclear reactors need new materials in order to face the extreme loading conditions encountered in terms of temperature and irradiation [above 923 K (650 °C) and up to 150 DPA]. For Sodium Fast Reactors (SFR), that is the most achieved solution for fast neutron technology, the choice of stainless steels is made for the fuel cladding material. Materials with a ferritic structure (body-centered cubic) exhibit a better resistance to swelling under irradiation [1]. In order to exceed the well-known poor creep properties of ferritic stainless steels, reinforcement is needed. Therefore, advanced ODS ferritic stainless steels containing a very high density of Y–Ti–O nano-precipitates are promising candidates for future high burn-up reactors [2]. Most of ODS alloys are produced by Mechanical Alloying (MA) of a base metallic powder with oxide powder. Then, the material is commonly consolidated by Hot Isostatic Pressing (HIP) or hot extrusion (HE) as a rough shape component before further hot/cold forming operations [3–5]. The control of the final mechanical properties resulting from numerous processing steps is a big challenge for the development of these materials. Conventional ferritic grades are known to present a reduced propensity to Discontinuous Dynamic Recrystallization (DDRX) [6] and undergo instead Continuous Dynamic Recrystallization (CDRX) during hot deformation [7–10]. Therefore, after transformation, the ODS microstructure usually exhibits strong morphologic and crystallographic textures [11–13].

In the present study, the objective is to investigate the possibility of tuning final microstructures and properties by playing on the loading path and the precipitation state. Final grain shape and crystallographic texture are of particular interest since they impact the mechanical anisotropy of the product. Controlling these microstructure features would allow to adjust circumferential properties of cladding tubes, which are currently too low as compared to the longitudinal ones [12].

During hot forming, a competition between intragranular and intergranular accommodation is assumed. The loading path can change the relative activities of competing deformation mechanisms, and this includes the effect of hydrostatic pressure. Using hot extrusion instead of hot torsion [14] allows achieving much larger strains without damage, and can modify the competition between the two mechanisms.

Three ferritic stainless steels are investigated in order to evaluate the impact of a dense precipitation on deformation mechanisms during hot extrusion. For this purpose, samples extracted at various positions along a flow line of an interrupted extrusion test were prepared, and the resulting microstructures were analyzed by Electron Back-Scattered Diffraction (EBSD).

The chosen initial microstructures have different grain sizes, and some of them have a bimodal grain size distribution. Larger grains tend to concentrate deformation and are therefore subjected to larger strain rates, compared to the smaller grains. Large strain rates, like low temperature, favor intragranular dislocation glide activity. The intensity of CDRX, which is related to this activity, is consequently influenced by this competition.

The document investigates the effects of loading path and initial precipitate structure on the final microstructure after hot extrusion. Loading path effects are discussed by comparison with the previously studied torsion tests [14].

Experimental procedure

Materials

The chemical compositions of the investigated ferritic steels are given in Table 1.

Processing

The studied ODS steels were produced by powder metallurgy from two gas-atomized pre-alloyed powders delivered by *Aubert and Duval*. For the Y–ODS alloy, the Un-Strengthened (US) powder was mechanically milled with 0.25 wt% Y_2O_3 and 0.3 wt% TiH_2 particles, in an attritor under hydrogen atmosphere, by *PLANSEE* company. The resulting powder has a mean particle size of about 80 μm. The second gas-atomized powder, already containing Ti, was milled, without added oxides, in an attritor under argon atmosphere at CEA to obtain the Ti–ODS alloy. The mean size of the milled powder was about 300 μm. The US base material, with a powder particle mean size of about 250 μm, was also consolidated but

Table 1 Nominal chemical composition, in wt%, of the grades characterized in the study

Material	Fe	Cr	W	Ti	Y_2O_3
Y–ODS	Bal.	14	1	0.3	0.25
Ti–ODS	Bal.	14	1	0.4	–
Un-strengthened (US)	Bal.	14	1	–	–

without prior milling. The three studied alloys were extruded at 1373 K (1100 °C) following the same operating procedure. A soft steel can was filled with the obtained powder, capped, and arc welded. The billet was then vacuumed at 673 K (400 °C) during 2 h and subsequently preheated at 1373 K (1100 °C) for 1 h before hot extrusion. The heating rate was about 1 K s^{-1}, corresponding to a dwell time at 1373 K (1100 °C) of around 40 min. The precipitation of nano-oxides occurred during this step [15]. The billet was hot extruded using a vertical 575 tons press at CEA. The extrusion ratio was 13:1, and the extrusion ram speed was 20 mm/s. This leads to local peak strain rates around 25 s^{-1} during forming [16].

In order to investigate microstructure evolution during HE, interrupted extrusions were performed. The ram displacement was stopped to preserve a part of the material in the upstream of the die. The obtained billet was extracted from the container and cut along the extrusion axis by electric discharge machining wire cutting. Figure 1a shows a cross section of the billet along the symmetry axis. The ODS steel is enclosed into the can. During the extrusion flow, material points are moving on identifiable streamlines. Consequently, evolutions induced by HE can be observed by selecting regions belonging to the same streamlines. This strategy enables the microstructural observations of material points at various stages of the process.

Microstructure characterization

EBSD measurements of different zones of the extruded billet were performed in order to determine the grain and sub-grain structure. The samples were extracted from the central axis, referred to LC. Figure 1b illustrates the positions of characterized samples. The associated number evolves from (1), initial state of the billet to (4), fully extruded material, the *Y*-axis showing the extrusion direction. Specimens were prepared by mechanical polishing. The measurements were carried out using a JEOL 7001-FLV scanning electron microscope equipped with Field Emission Gun and operating at an accelerating voltage and working distance of 20 kV and 15 mm, respectively. The step size was chosen as a function of the grain size. It was 50 nm for the Y–ODS material, 400 nm for the Ti–ODS material, and 600 nm for the US material. In this work, high-angle grain boundaries (HABs) are defined by misorientations higher than 10° and low-angle boundaries (LABs) by misorientations from 2° to 10°. A minimum misorientation cutoff of 2° has been used to avoid excessive misorientation noise. A grain is defined by at least four pixels. For each state, the microstructure is shown within an orientation color-code (extrusion direction, ED, projected in the standard stereographic triangle) presented in Fig. 8. Orientation Distribution Functions (ODFs) are computed using the Fourier series expansion method with a half bandwidth of 5°. Texture indexes are determined via the J-index of Bunge [17] after reconstruction of pole figures. X-ray diffractions are obtained on a BRUCKER X'Pert Pro diffractometer with a Co source. The measurements were carried out on the same samples as for the EBSD characterizations.

Precipitation

Size and density of precipitates are analyzed on consolidated samples using a FEG-TEM (JEOL JEM-2010F) operating at 200 kV. Figure 2 presents the distribution of precipitates diameters for the Y–ODS and Ti–ODS obtained from measurements carried out on TEM images of about 400 precipitates. For the Y–ODS grade, nanoscale precipitates are observed, which is not the case in Ti–ODS. For the first one the size distribution is narrow, with a mean size and a number density of about 2–3 nm and 5×10^{22} m^{-3}, respectively (Fig. 2), whereas the second one exhibits a wider distribution (from 10 to 160 nm) for a mean size and number density of 45 nm and 1.3×10^{20} m^{-3}, respectively.

Table 2 calculates, from the number density, the distance between particles on a gliding plane according to the work of Ukai [19], as well as the *volume fraction/radius* ratio which matters for the Zener pinning effect at grain boundaries. The Y–ODS and Ti–ODS grades differ mainly by the distance between precipitates; the Zener pinning effect is comparatively closer. It is therefore expected that dislocation glide will be significantly favored in the

Figure 1 Geometry of the hot extrusion **a** cross section of the extruded part, **b** positions of the characterized samples.
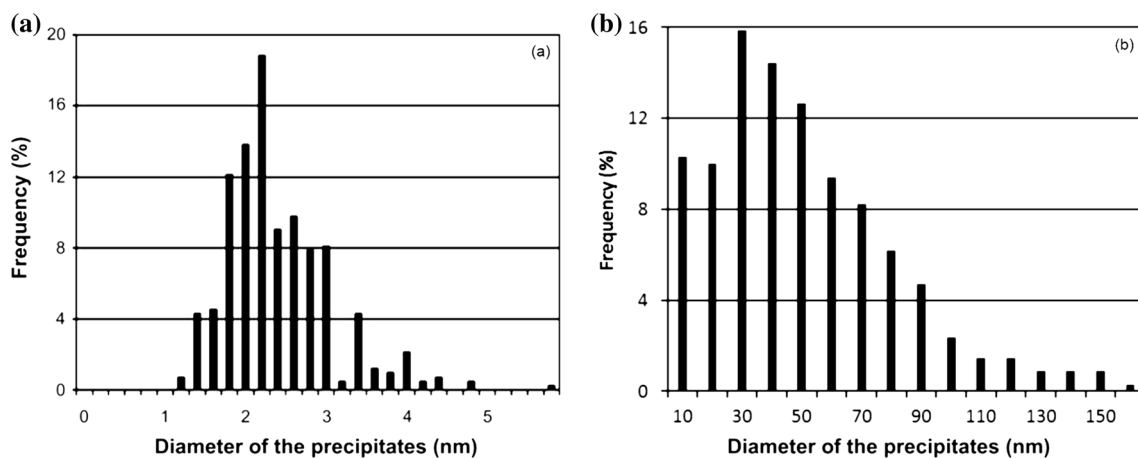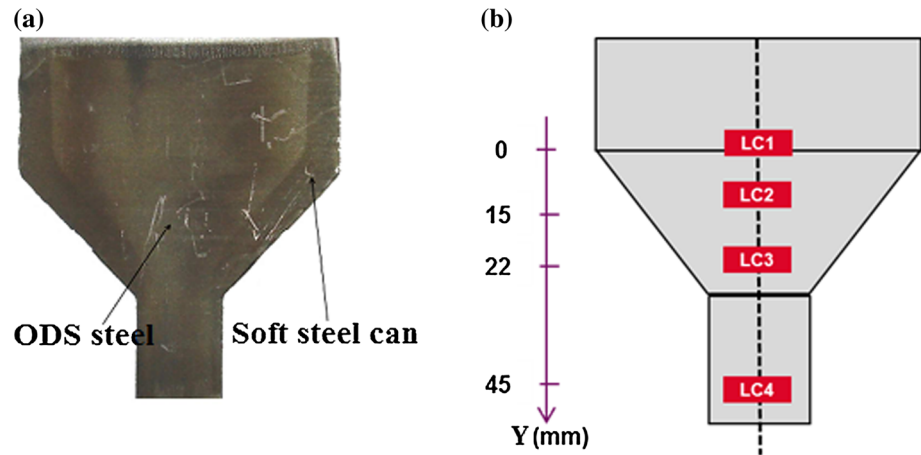

(a)

ODS steel   Soft steel can

(b)

LC1

LC2

LC3

LC4

0

15

22

45

Y (mm)

Figure 2 Precipitates size distribution for **a** the **Y–ODS** according to [18] and **b** the **Ti–ODS**.

Ti–ODS, compared to Y–ODS. The influence of the martensite phase in the US grade is also estimated from EBSD map data (Fig. 8).

Results

Y–ODS alloy

Figure 3 shows the EBSD maps obtained at different positions of the central flow line. The extrusion direction is indicated by a black arrow in the top right of each map. Before extrusion (LC1), the microstructure consists of a mixture of fine submicron grains and large grains without any crystallographic texture. With increasing deformation, the large grains elongate in the extrusion direction and develop a low-angle grain boundaries structure, together with an α-fiber crystallographic texture (<110>//extrusion direction). The proportion of grains with an α-fiber orientation (green color) increases progressively. These grains tend to fragment and form low-angle grain boundaries; the fragmentation process can even lead to new grains, i.e., high-angle grain boundaries.

Table 2 Distance between precipitates and volume fraction to radius ratio for the different grades. Martensite phases are considered for the US grade

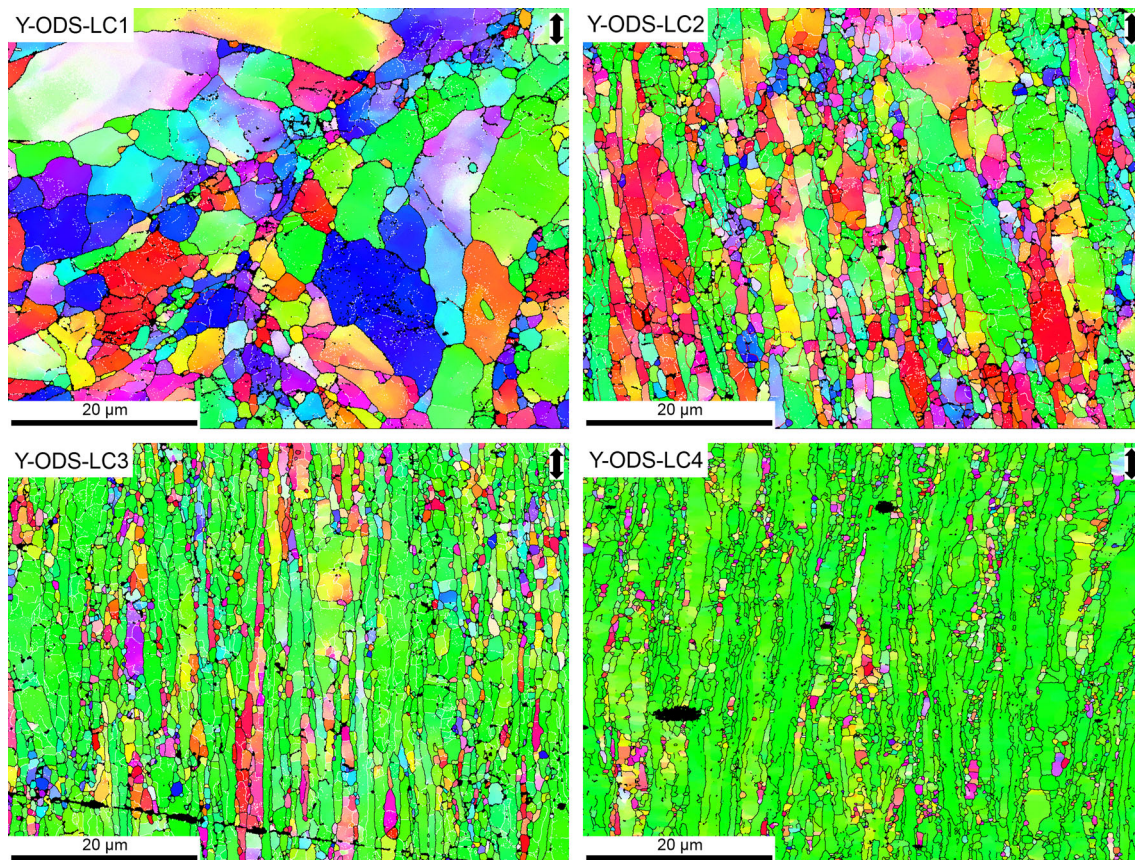| Grade	Distance between precipitates (nm)	Fv/r ratio (nm^{-1})
Y–ODS	110	3.3×10^{-2}
Ti–ODS	480	2.8×10^{-2}
US	$\approx 3 \times 10^{4}$	$\approx 1 \times 10^{-5}$

Figure 3 IPF maps showing the microstructure evolution from LC1 to LC4 during the hot extrusion of **Y–ODS** alloy. Black arrows on maps indicate the extrusion direction. The colored reference IPF map is specified on Fig. 8 (IPF_ED).

Both populations of equiaxed and elongated grains are observed in the fully extruded sample (LC4). At this stage, the α-fiber orientation is almost uniform, at the exception of the small remaining equiaxed grains.

The statistical evaluation of the EBSD results, providing the average grain size and aspect ratio in the different samples, is presented in Fig. 4. Considering a size threshold of 1 µm, the grains are separated into two groups. For each map, the analyses were done for the entire data set, and within the two grain populations considered separately.

The two grain populations do not exhibit the same evolution with deformation. Fine grains keep almost the same morphology and size, while the large grains elongate considerably up to an aspect ratio of about 3.5, and reduce their size. The global trend to grain refinement therefore essentially reflects the behavior of the large grains population: The mean grain size is dropping from 2.1 µm before extrusion to about 0.7 µm in the extruded material (Fig. 4a).

Figure 5 presents the parallel evolution of LABs and HABs (Fig. 5a), and the distribution of LABs misorientation angles (Fig. 5b) for different positions along the LC axis.

The observed evolution of LABs under increasing strain is consistent with the occurrence of CDRX [7, 20]. Simultaneously, the HABs proportion increases and seems to reach a steady state from the LC3 position. The progressive increase of HABs from LC1 to LC3 is related to the progressive transformation of LABs into HABs. Looking at both LABs and HABs evolutions and grain refinement, one can conclude with no ambiguity that CDRX is active during the hot extrusion process, at least for the large grains population.

Ti–ODS alloy

Figure 6 shows the evolution of the microstructure of a Ti–ODS alloy during hot extrusion at 1373 K (1100 °C). The initial state (Ti–LC1) shows a bimodal grain size distribution consisting of fine grains and
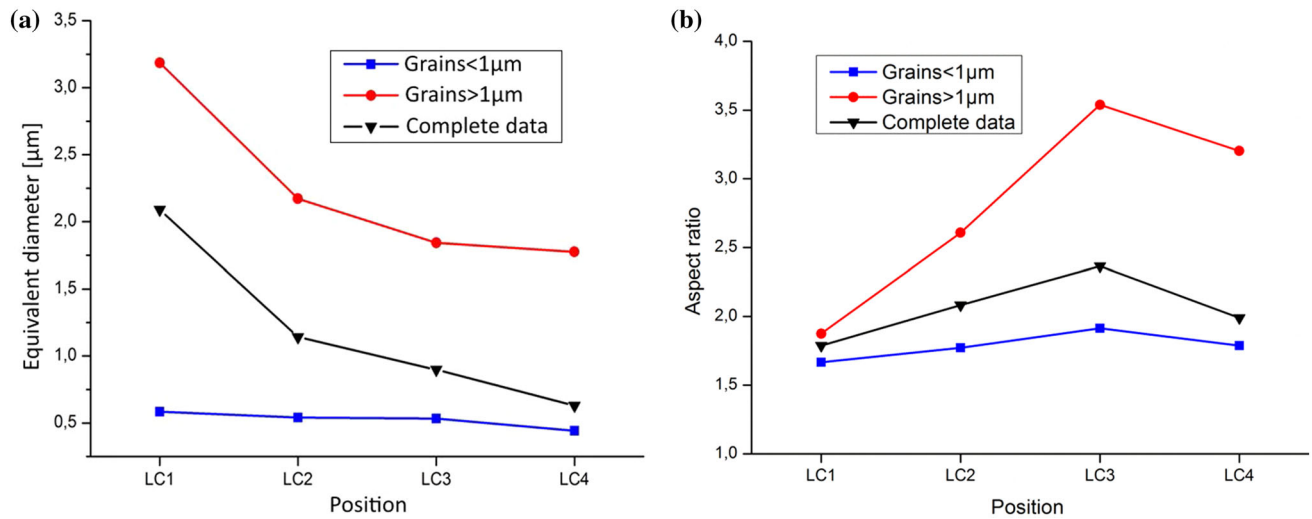
Figure 4 Evolution during extrusion of, **a** the average size and **b** the aspect ratio of small and large grain populations. Complete data corresponds to the whole map.
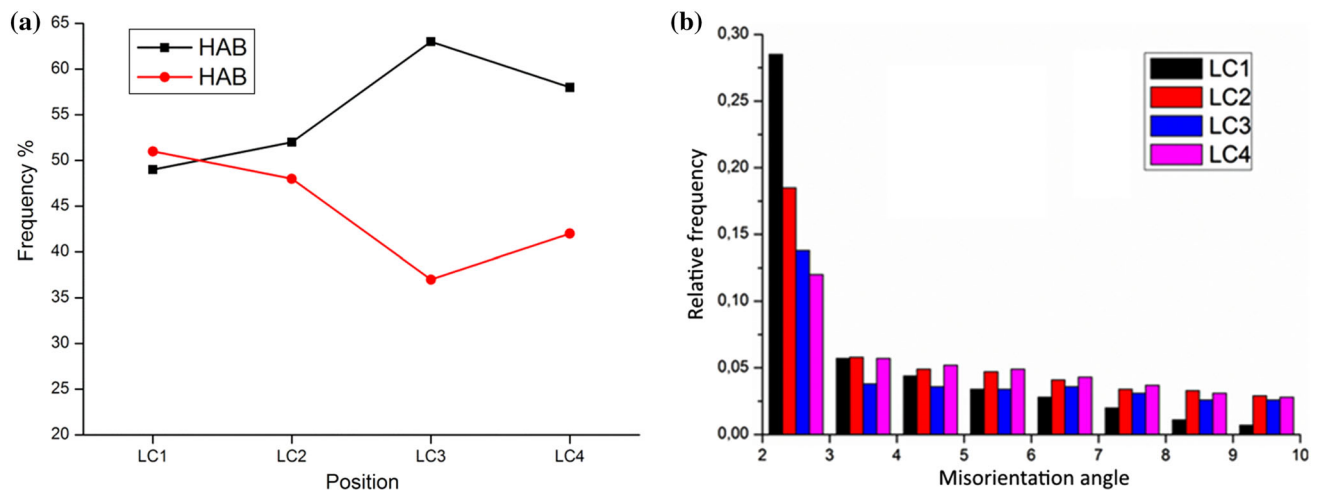

Figure 5 **a** Evolution of the LABs and HABs frequencies and **b** LABs distribution during the extrusion.

coarse grains with no preferential crystallographic orientation. In the early stages of extrusion, a significant microstructure evolution is observed.

Grains are elongated along the material flow direction, and fragmented into new grains. As shown in Fig. 7, the grain size decreases during the process, leading to a refinement of the microstructure. A slight decrease of the average aspect ratio after LC2 position is also noticed, probably resulting from the fragmentation of the grains. As for the Y–ODS, the Ti–ODS grade deformation leads to a transformation of LABS into HABs (Fig. 7), which, together with the

grain refinement, is consistent with the occurrence of CDRX.

Un-strengthened alloy

Figure 8 shows the microstructure evolution of the atomized base powder without strengthening. For this alloy, a dual-phase microstructure composed of large equiaxed ferritic grains and martensitic domains (corresponding to the black areas in the EBSD maps, with a volume fraction around 10%) is observed. Existence of martensite in such a material considered as purely ferritic is surprising. However,
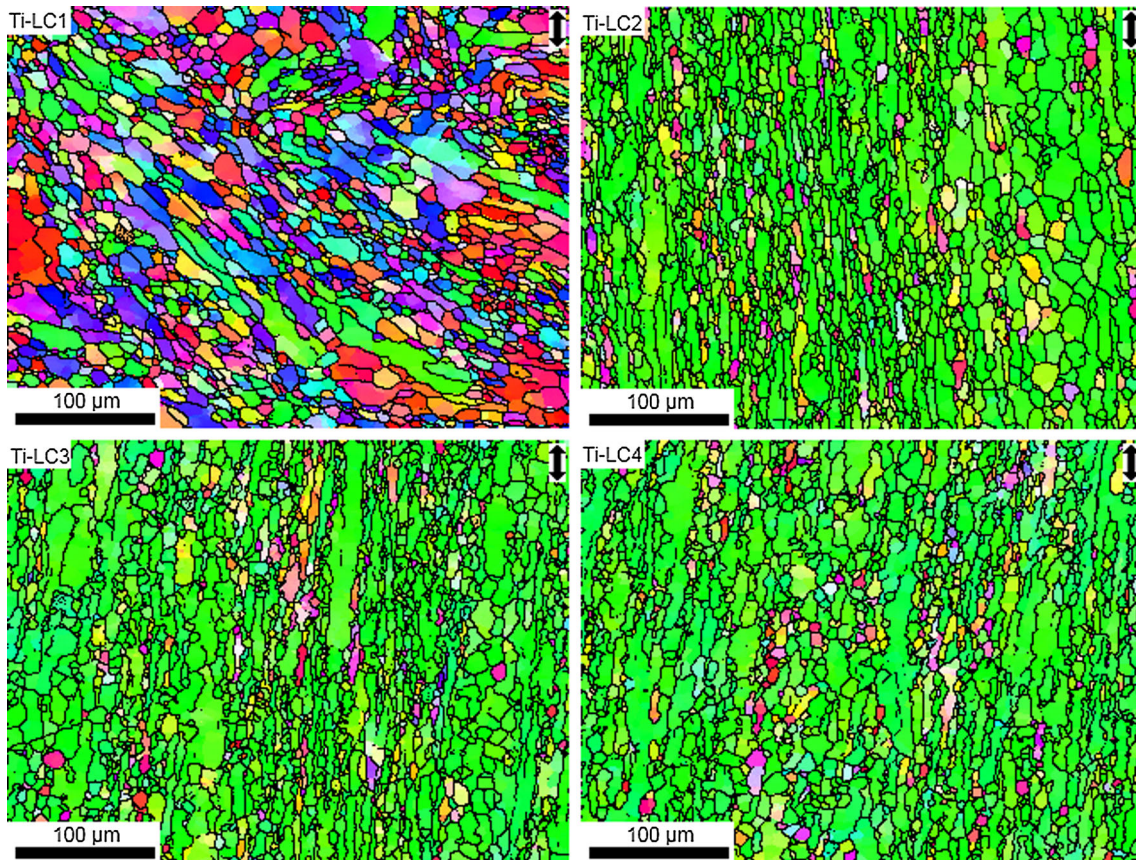
Figure 6 IPF maps showing the microstructure evolution from LC1 to LC4 during the hot extrusion of the **Ti–ODS** alloy. The colored reference IPF map is specified on Fig. 8 (IPF_ED).
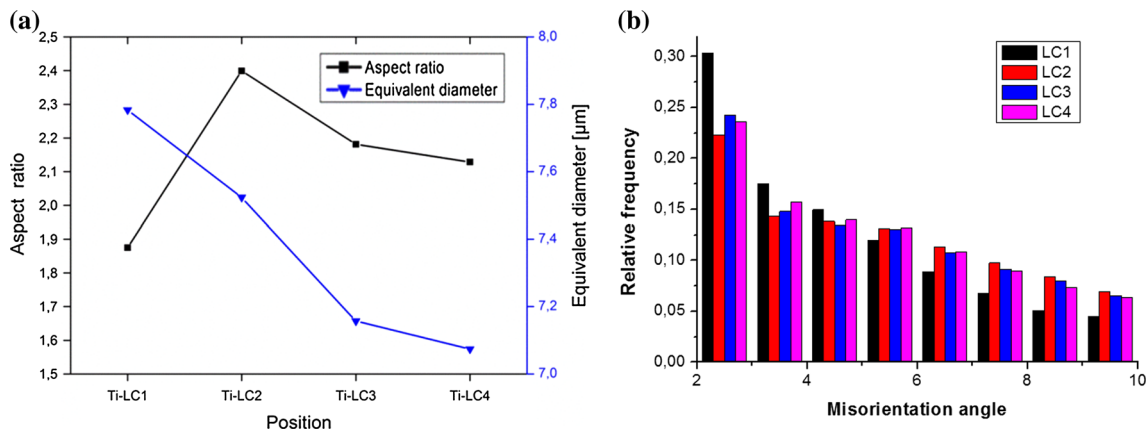

Figure 7 **a** Evolution of the average grain morphology during extrusion. **b** LABs distribution during the extrusion.

this phenomenon can be explained by the existence of a two phase domain at high temperature, for this grade without titanium. Due to higher solubility of carbon in austenite than in ferrite, dwell time at high temperature leads to carbon segregation into austenite. Therefore, during cooling, some regions enriched with carbon are transformed into

martensite. The forming temperature is above AC1, consequently, austenite and ferrite ($\gamma + \alpha'$) regions are both present during HE. During deformation, the ferritic grains keep their equiaxed shape, but they develop a preferential <110> crystallographic orientation along the extrusion direction. A microstructure refinement is also noticed; the mean grain diameter
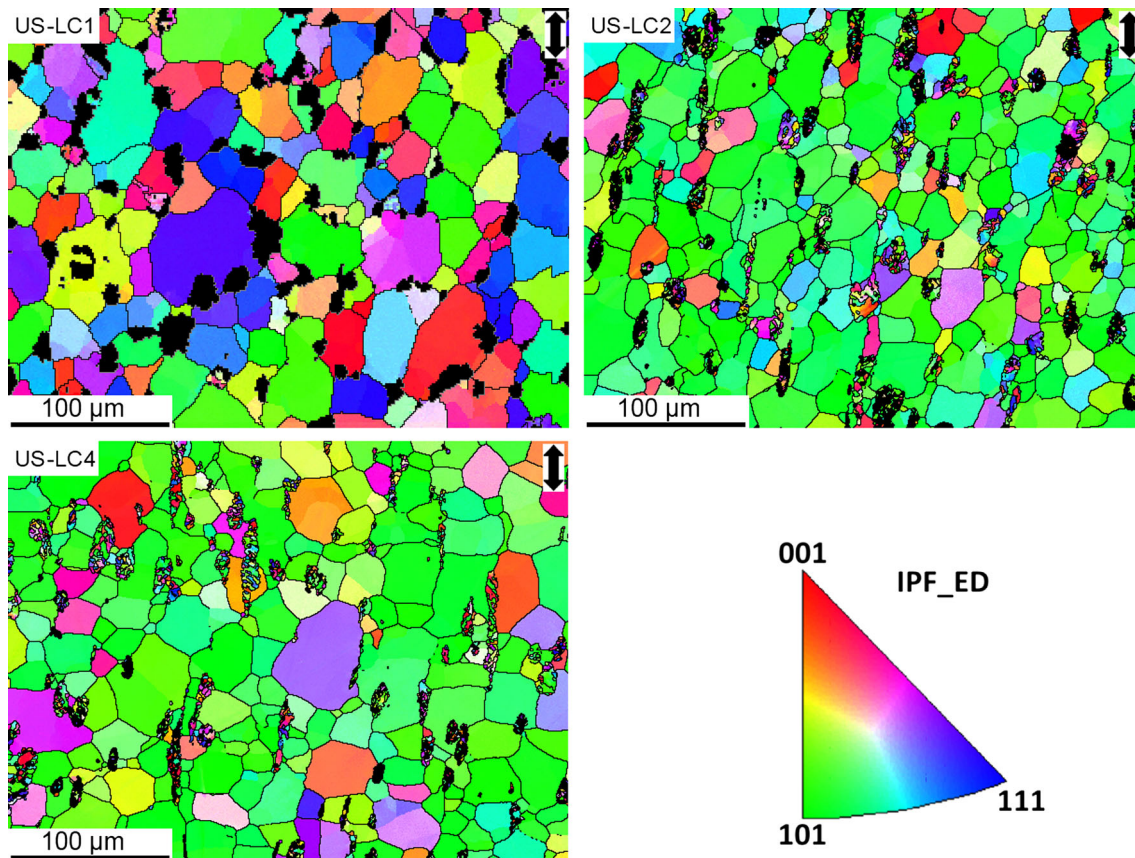
Figure 8 IPF maps showing the microstructure evolution during hot extrusion of the atomized powder. (LC1) Initial state, (LC2) intermediate state, (LC3) extruded states, and (IPF-ED) the orientation color-code map with respect to the extrusion direction.

decreases from 26 μm at LC1 position to about 22 μm after extrusion. The martensitic domains, however, elongate in the material flow direction. These observations indicate a very active continuous dynamic recrystallization in the ferritic grains. The formation of a strong texture is also consistent with the occurrence of CDRX.

Crystallographic texture evolution

Orientation Distribution Functions (ODFs) are computed, and the corresponding inverse pole figures are plotted in Fig. 9. Before extrusion (LC1 position), all materials present essentially a random texture. A smooth (<111>//ED) reinforcement is noticed for the Y–ODS material. After deformation, the well-known α fiber (<110>//ED) commonly generated by hot extrusion in BCC alloys is observed for the three materials.

The texture index versus the cumulated plastic strain induced by hot extrusion is plotted in Fig. 10.

The cumulated plastic strain corresponding to LC1–LC4 positions is determined by finite element simulations [16]. For Y–ODS, the texture index increases proportionally to the amount of strain, whereas for the two other grades, saturation seems to appear from LC2 to LC4 positions. Texture indexes obtained by XRD (dotted line in Fig. 10) show the same tendency as the ones obtained by EBSD except for the first sample. Observed differences can be explained by the choice of the half-width angle during EBDS data treatment. As an attempt to reach the Y–ODS maximum texture index, this grade has been extruded with a higher extrusion ratio ($R = 17:1$ vs 13:1). The points, circled in Fig. 10, indicate that the maximum texture index is reached for a value of about seven. Overall, the texture index appears to increase with deformation until a critical value is reached, which can be related to precipitates density.
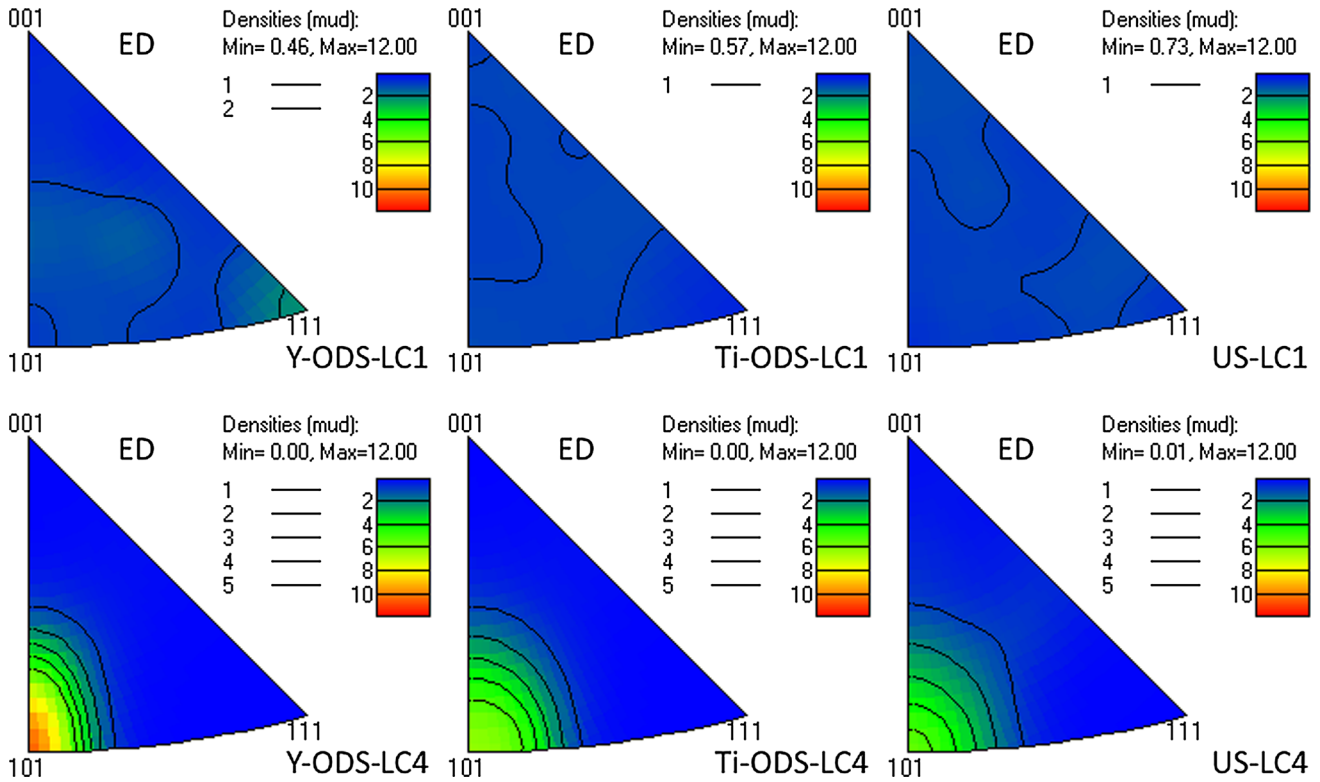
Figure 9 Inverse poles figures, with respect to the Extrusion Direction (ED) of the initial state LC1 (first line) and extruded state LC4 (second line) for the different materials.
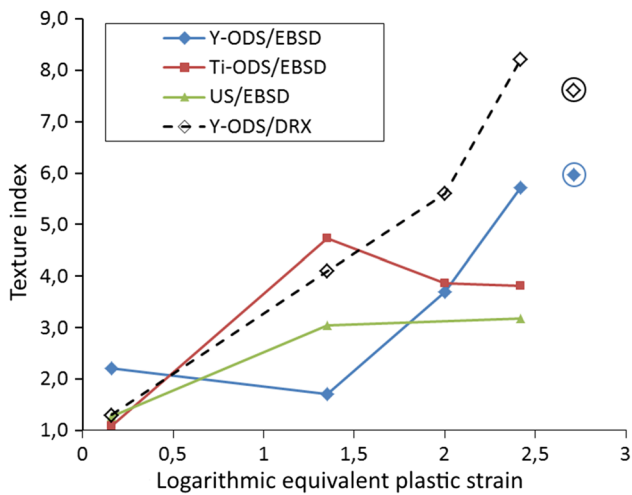

Figure 10 Texture indexes as function of cumulated plastic strain.

Discussion

The previous study focusing on torsion tests [14] shows a clear occurrence of damage at grain boundaries, with a negligible impact of plastic straining on grain morphology and crystallographic texture. A grain boundary accommodation phenomenon was proposed to explain the observed behavior. Unfortunately, the early development of damage leads to failure before achieving very high strain levels (strains to failure being around 1). In this study, the high stress triaxiality induced by hot extrusion avoids damage development [21], up to strains of 2.5 (see Fig. 10).

Considering the mean distance between precipitates (Table 2), the ease of dislocation motion is maximum in the US grade, and strongly reduced in the Y–ODS one. At the same time, the *volume fraction/radius* ratio indicates that Zener pinning effects are almost the same for Ti–ODS and Y–ODS, and 1000 time lower for the US grade. Easy dislocation motion means more intragranular dislocation glide, and therefore more transformation of LABs into HABs, i.e., more active CDRX. Simultaneously, Zener pinning pressure limits grain boundary motion, which also promotes CDRX.

From the above analysis, one can conclude that CDRX is more active in the Ti–ODS grade, compared to the Y–ODS grade: Zener pining is similar (and high), but gliding is easier in Ti–ODS. Comparison

with the US grade is not as straightforward, as both gliding and grain boundary motion are easier in the latter, i.e., two effects oppose each other.

Grain size and grain shape evolutions during forming result from a competition between CDRX and gain boundary motion. A more active CDRX tends to reduce grain size and limits the grain aspect ratio, while grain boundary motion tends to increase grain size. Comparing Ti–ODS with Y–ODS grades, one can then understand the higher grain aspect ratios (Figs. 7a vs 4b) and stronger grain refinement (Figs. 7a vs 4a) in Y–ODS, due to the less active CDRX, and reduced grain boundary motion, respectively. One can notice that, in the investigated conditions, grain boundary motion has the major influence on grain size, i.e., the influence of CDRX is comparatively lower. This is confirmed when looking at the US grade results, where grain size remains very large at all deformation stages, despite the very active CDRX which prevents grain elongation.

The texture index is an indicator of intragranular dislocation glide, which can be measured here by the strength of the α-fiber. Both CDRX and grain boundary migration can weaken deformation induced textures, which explains some of the results in Fig. 10, in particular the saturation of the texture index at increasing plastic strain for Ti–ODS and US grades.

Focusing on the Y–ODS grade, it appears that small grains (less than 1 μm) do not form a texture, and do not elongate (Fig. 4). Therefore, we assume that plastic glide is limited in the bulk of those grains and that deformation is mainly accommodated at grain boundaries. Coexistence of textured/elongated grains and small/equiaxed ones, even at large strains, proves that standard intragranular plasticity competes with grains boundary accommodation in the investigated range of temperature and strain rate (1373 K (1100 °C) and 25 s^{-1}). The observed competition between intragranular and intergranular deformation mechanisms in the considered ODS materials, as a function of grain size, is consistent with the work of Stoica et al [22]. This latter study shows, for tensile tests at about 50% straining, a transition from low temperatures (until 400 °C) intragranular dislocation gliding mechanism, to another one mediated by grain boundary accommodation, at higher temperatures (from 600 °C).

The reduced dislocation glide activity in smaller grains can be explained by the reduced strain rate in these grains, since their flow stress is higher, and by

arguments similar to those used for nanocrystalline materials [23, 24]. It is well understood that submicron grains in ODS materials remain significantly larger than those encountered in nanocrystalline materials and for which intergranular accommodation starts dominating over bulk dislocation glide. However, as already discussed, the high precipitates density in the ODS materials plays an important role in suppressing dislocation glide. This can affect not only the level of CDRX, but also the critical grain size below which grain boundary accommodation becomes dominant.

Conclusion

Microstructure evolution during hot extrusion of three ferritic steels, obtained from powder metallurgy, was investigated. The results can be summarized as follows:

- Continuous dynamic recrystallization occurs during hot extrusion of all studied ferritic steels. By a comparative analysis of the different materials, the precipitation state is shown to influence the kinetics of CDRX, grain boundary motion, and therefore grain size and grain shape. When precipitates density is very large (Y–ODS), dislocation motion is hindered, which makes the formation of LABs and the progressive increase of their misorientation more difficult. Grain boundary motion is also limited by Zener pinning effects. In the Ti–ODS and non-ODS materials, CDRX is easier, and Zener pinning is reduced, resulting in larger, more uniform grain size, and more equiaxed grain shapes.

- During extrusion of the Y–ODS alloy, fine grains show little evolutions while the large grains elongate in the flow direction, undergo CDRX, and form a strong α-fiber texture. The different behavior of these two types of grains is attributed to a competition between intragranular and intergranular deformation mechanisms, the latter becoming dominant in the smallest grains.

- Analogies can be drawn between the observed ODS materials behavior and the one reported for nanocrystalline metals. In particular, the concept of critical grain size below which intergranular accommodation dominates over bulk dislocation glide appears to apply also to the studied ODS

ferritic steels, with, however, a larger critical grain size due to the high density of fine precipitates.

- All extruded materials show a strong crystallographic α-fiber texture. The observed differences in texture evolutions for the various grades can be explained by the extent of CDRX and grain boundary motion, and by the competition between the two identified deformation mechanisms.

Acknowledgements

References

[1] Yvon P, Carre F (2009) Structural materials challenges for advanced reactor systems. J Nucl Mater 3852:217–222

[2] Ukai S, Konings RJM (2012) 4.08—Oxide dispersion strengthened steels. Comprehensive nuclear materials. Elsevier, Oxford, pp 241–271

[3] Olier P, Bougault A et al (2009) Effects of the forming processes and Y_2O_3 content on ODS-Eurofer mechanical properties. J Nucl Mater 386–388:561–563

[4] Ukai S, Hatakeyama K, Mizuta S (2002) Consolidation process study of 9Cr–ODS martensitic steels. J Nucl Mater 307–311:758–762

[5] Oksiuta Z, Lewandowska M, Kurzydlowski KJ, Baluc N (2011) Influence of hot rolling and high speed hydrostatic extrusion on the microstructure and mechanical properties of an ODS RAF steel. J Nucl Mater 409:86–93

[6] Gourdet S, Montheillet F (2003) A model of continuous dynamic recrystallization. Acta Mater 51(9):2685–2699

[7] Humphreys FJ, Hatherly M (2004) Recrystallization and related annealing phenomena. Elsevier, Amsterdam

[8] Castan C, Montheillet F, Perlade A (2013) Dynamic recrystallization mechanisms of an Fe—8% Al low density steel under hot rolling conditions. Scripta Mater 68(6):360–364

[9] Sakai T, Belyakov A, Kaibyshev R, Miura H, Jonas JJ (2014) Dynamic and post-dynamic recrystallization under hot, cold and severe plastic deformation conditions. Prog Mater Sci 60:130–207

[10] Kim S-I, Yoo Y-C (2002) Continuous dynamic recrystallization of AISI 430 ferritic stainless steel. Met Mater Int 8:7–13

[11] Steckmeyer A, Praud M, Fournier B, Malaplate J, Garnier J, Béchade JL, Tournié I, Tancray A, Bougault A, Bonnaillie P (2010) Tensile properties and deformation mechanisms of a 14Cr ODS ferritic steel. J Nucl Mater 405(2):95–100

[12] Kasada R, Lee SG, Isselin J, Lee JH (2011) Anisotropy in tensile and ductile–brittle transition behavior of ODS ferritic steels. J Nucl Mater 417:180–184

[13] Serrano M, Hernandez-Mayoral M, Garcia-Junceda A (2012) Microstructural anisotropy effect on the mechanical properties of a 14Cr ODS steel. J Nucl Mater 428(1–3):103–109

[14] Karch A, Sornin D, Barcelo F, Bosonnet S, De Carlan Y, Logé R (2014) Microstructural characterizations of 14Cr ODS ferritic steels subjected to hot torsion. J Nucl Mater 459:53–61

[15] Boulnat X, Sallez N, Dadé M, Borbély A, Béchade JL, de Carlan Y, Malaplate J, Bréchet Y, de Geuser F, Deschamps A, Donnadieu P, Fabrégue D, Perez M (2015) Influence of oxide volume fraction on abnormal growth of nanostructured ferritic steels during non-isothermal treatments: an in situ study. Acta Mater 97:124–130

[16] Sornin D, Karch A, Nunes D (2015) Finite element method simulation of the hot extrusion of a powder metallurgy stainless steel grade. Int J Mater Form 8:145–155

[17] Bunge HJ (1982) Texture analysis in materials science. Butterworth-Heinemann, London, p 593

[18] Praud M, Mompiou F, Malaplate J, Caillard D, Garnier J, Steckmeyer A, Fournier B (2012) Study of the deformation mechanisms in a Fe-14% Cr ODS alloy. J Nucl Mater 428(1–3):90–97

[19] Ukai S (2011) Microstructure and high temperature strength of 9Cr ODS ferritic steel. In: Cuppoletti J (ed) Metal, ceramic and polymeric composites for various uses, p 698

[20] Gourdet S, Montheillet F (2000) An experimental study of the recrystallization mechanism during hot deformation of aluminium. Mater Sci Eng A 283:274–288

[21] Bao Y, Wierzbicki T (2005) On the cut-off value of negative triaxiality for fracture. Eng Fract Mech 72(7):1049–1069

[22] Stoica GM, Stoica AD, Miller MK, Ma D (2014) Temperature-dependent elastic anisotropy and mesoscale deformation in a nanostructured ferritic alloy. Nat Commun 5:5178

[23] Shen X, Lian J, Jiang Q (2008) High strength and high ductility of electrodeposited nanocrystalline Ni with a broad grain size distribution. Mater Sci Eng, A 487:410–416

[24] Van Swygenhoven H, Weertman JR (2006) Deformation in nanocrystalline metals. Mater Today 9:24–31